SANDIA REPORT

SAND2013-10305
Unlimited Release
December 2013

Theoretical and Experimental Studies of Electrified Interfaces Relevant to Energy Storage

Jeremy A. Templeton, Reese E. Jones, Jonathan W. Lee, Kranthi K. Mandadapu, Christopher J. Kliewer, Darryl Y. Sasaki, Marie Kane, Karla R. Reyes, Carl C. Hayden

Prepared by
Sandia National Laboratories
Albuquerque, New Mexico 87185 and Livermore, California 94550

Sandia National Laboratories is a multi-program laboratory managed and operated by Sandia Corporation, a wholly owned subsidiary of Lockheed Martin Corporation, for the U.S. Department of Energy's National Nuclear Security Administration under contract DE-AC04-94AL85000.

Issued by Sandia National Laboratories, operated for the United States Department of Energy by Sandia Corporation.

Available to DOE and DOE contractors from
U.S. Department of Energy
Office of Scientific and Technical Information
P.O. Box 62
Oak Ridge, TN 37831

Telephone: (865) 576-8401
Facsimile: (865) 576-5728
E-Mail: reports@adonis.osti.gov
Online ordering: http://www.osti.gov/bridge

Available to the public from
U.S. Department of Commerce
National Technical Information Service
5285 Port Royal Rd.
Springfield, VA 22161

Telephone: (800) 553-6847
Facsimile: (703) 605-6900
E-Mail: orders@ntis.fedworld.gov
Online order: http://www.ntis.gov/help/ordermethods.asp?loc=7-4-0#online

SAND2013-10305
Unlimited Release
December 2013

Theoretical and Experimental Studies of Electrified Interfaces Relevant to Energy Storage

Jeremy A. Templeton,[1] Reese E. Jones,[2] Jonathan W. Lee,[1] Kranthi K. Mandadapu,[1]
Christopher J. Kliewer,[3] Darryl Y. Sasaki,[4] Marie Kane,[5] Karla R. Reyes,[5] Carl C. Hayden[3]

[1]Thermal/Fluid Science and Engineering
[2]Mechanics of Materials
[3]Combustion Chemistry
[4]Biotechnology and Bioengineering
[5]Materials Chemistry

Sandia National Laboratories
P.O. Box 969
Livermore, CA 94551-MS9055

Abstract

Advances in technology for electrochemical energy storage require increased understanding of electrolyte/electrode interfaces, including the electric double layer structure, and processes involved in charging of the interface, and the incorporation of this understanding into quantitative models. Simplified models such as Helmholtz's electric double-layer (EDL) concept don't account for the molecular nature of ion distributions, solvents, and electrode surfaces and therefore cannot be used in predictive, high-fidelity simulations for device design. This report presents theoretical results from models that explicitly include the molecular nature of the electrical double layer and predict critical electrochemical quantities such as interfacial capacitance. It also describes development of experimental tools for probing molecular properties of electrochemical interfaces through optical spectroscopy. These optical experimental methods are designed to test our new theoretical models that provide descriptions of the electric double layer in unprecedented detail.

ACKNOWLEDGMENTS

This work was funded under LDRD Project Number 151338, Titled "Theoretical and Experimental Studies of Electrified Interfaces Relevant to Energy Storage."

Contents

Figures

NOMENCLATURE

3CM	Three component model
CCD	charge-coupled device
c-DFT	classical Density Functional Theory
CDL	composite diffuse layer
CVD	chemical vapor deposition
EDL	Electric double layer
EFISH	electric field induced second harmonic
EOF	Electro-osmotic flow
FCC	face centered cubic
f-DFT	fluid Density Functional Theory
FTIR	Fourier-transform infrared
HCP	hexagonal closest packed
LJ	Lennard-Jones
MBP	modified Poisson-Boltzmann
MC	Monte Carlo
MD	Molecular dynamics
MSA	Mean Spherical Approximation
MSM	molecular solvent model
PB	Poisson−Boltzmann
PM	primitive model
PM-RAIRS	Polarization modulation reflection absorption infrared spectroscopy
RPM	restricted primitive model
SAM	self-assembled monolayer
SERS	surface-enhanced Raman spectroscopy
SHG	Second harmonic generation

1. INTRODUCTION

Major advances in electrochemical technologies for energy storage require improved understanding of electrolyte/electrode interfaces, including structure, interfacial species, and electrochemical processes, and the incorporation of this understanding into quantitative models. Such models will guide development of advanced designs and materials to increase efficiency and reduce aging and failure rates. Simplified models such as Helmholtz's electric double-layer (EDL) concept and even Gouy-Chapman-Stern's diffuse model fail to take into account the molecular nature of ion distributions, solvents, and electrode surfaces and therefore cannot be used in predictive, high-fidelity simulations for device design. The goal of this project is to develop detailed models of the structure and chemical properties of representative electrified interfaces, and to develop multiparameter, minimally invasive experimental measurements that are capable of validating these models. Such synergistic interaction between calculations and experiment is only now becoming possible with Sandia's rapid development of atomistic-to-continuum interfacial modeling and recent advances in spatially precise in-situ optical probes enabled by emerging laser technology. Much of previous work in this field has focused on complex, integrated electrochemical energy-storage devices and/or materials that are not suitable for detailed modeling and in-situ probing. Our approach attempts to gain a predictive understanding of complex interfaces present in such devices through coordinated experimental and theoretical studies of tractable (model) systems, which isolate important phenomena. Our modeling studies have developed a robust understanding of packing structure and EDL capacitance in existing coarse-grained particle models. We have demonstrated that existing coarse-grained models over-predict EDL capacitance by a factor of 20 versus higher-fidelity (more realistic) models, and proved that molecular structure is important in the double layer to accurately predict capacitance Experimentally we have developed several laser-based technologies capable of probing interfacial electric fields and identification of species at the interface. Raman microscopy and polarization modulation reflection absorption infrared spectroscopy (PM-RAIRS) were implemented to identify species and to measure electric field effects through surface vibrational spectroscopy. The availability of a new high power femtosecond laser in the last year of the project enabled the development of surface sensitive second harmonic generation (SHG) spectroscopy for determining how electric fields affect

optical properties at interfaces. These experimental capabilities complement our development of unique theoretical methods to model these interfacial optical properties.

2. COMPARISON OF MOLECULAR DYNAMICS WITH CLASSICAL DENSITY FUNCTIONAL AND POISSON−BOLTZMANN THEORIES OF THE ELECTRIC DOUBLE LAYER IN NANOCHANNELS

This section contains highlights of a publication. For details see Lee, J. W.; Nilson, R. H.; Templeton, J. A.; Griffiths, S. K.; Kung, A.; and Wong, B. M.; "*Comparison of Molecular Dynamics with Classical Density Functional and Poisson−Boltzmann Theories of the Electric Double Layer in Nanochannels,"* J. Chem. Theory Comput. *8*, **2012**, 2012−2022.

2.1. Introduction

The structure of the electric double layer (EDL) on a charged surface has long been modeled using the Poisson−Boltzmann (PB) theory. PB incorporates Coulombic interactions among charged particles but treats them as point charges, neglecting their finite size. Although this omission is relatively unimportant at low charge densities, it permits physically unrealistic ion packing densities when the surface potential and charge density become large, as occurs for example in energy storage applications.[1] To treat this deficiency, a number of modified PB theories have been devised over the years[2] and have met with some success, though they lack the fundamental foundation needed to accommodate a broad range of molecular interactions.

Molecular dynamics (MD) simulation provides the most fundamental and flexible platform for analysis of molecular interactions. As such, it has been used rather extensively in modeling of electro-osmotic flow (EOF)[3−8] and to treat the higher charge densities of importance in EDL capacitors.[9−11] However, MD simulations entail considerable computational cost, making them impractical for treatment of time and length scales found in many applications. Difficulties also arise in applying boundary conditions and in computing long-range Coulombic interactions. For these reasons, alternative methods are still sought.

Alternative methods include modified PB approaches, integral equation methods, and classical Density Functional Theory (c-DFT). c-DFT, sometimes referred to as fluids DFT, yields the time-mean density distributions of molecular species that minimize a free energy functional.[12−17] The free energy at any point is defined by a density weighted integration of molecular pair potentials over the surroundings. Thus, c-DFT and MD are readily comparable given the same

pair potentials and input parameters. Unlike MD, however, c-DFT readily incorporates long-range Coulombic interactions as the product of ion charge with the electric potential obtained by solving Poisson's equation. In addition, the c-DFT formalism yields an expression for the chemical potential in terms of pair-potential integrals over the surrounding field. This chemical potential can be incorporated into existing finite element models of steady and transient transport processes, thus facilitating the introduction of atomistic physics into efficient multiscale models. Finally, c-DFT computing times are far shorter than those required for MD.

Unlike previous studies, our work compares c-DFT with MD results for a nonprimitive three component model (3CM), in which the solvent and ions are all treated as distinct molecular species differing in charge and size. In further contrast with prior work, 12−6 Lennard-Jones interactions among all species are included, and the wall interaction is modeled by the one dimensional Lennard-Jones 10−4−3 potential, as these are more realistic and more compatible with MD practice than hard interactions. In addition, the present comparisons are extended to considerably greater charge densities than previously explored, reaching into a range relevant to energy storage.

We view these increases in complexity and range of the EDL model as a first step toward validation of c-DFT in a more realistic setting. This step is in the direction of the more general MD studies of EOF[3−8] which also include the additional complexity of polar solvents, atomistically structured walls, and cross-flow. In the current work, MD simulations were performed for a large range of ion concentrations and for surface charge densities many times greater than is typical of EOF. In most cases, the bulk region can be clearly distinguished, thereby revealing the reference state needed for comparison with c-DFT. For the results of this paper, agreement between c-DFT and MD is deemed excellent, though it degrades somewhat with increasing charge density.

2.2. Comparison of c-DFT and MD Simulation of EDL

An overview comparison of computed surface potential versus surface charge density among our MD, our c-DFT, and classical PB modeling is provided by Figure 1. This is a very important metric as the inverse slope of this plot is the capacitance. Since kBT/e ≈ 25 mV, the upper range

of the potential slightly exceeds 1 V, typical of double layer capacitors. MD results (symbols) are shown for three charge densities (0.44, 0.88, and 1.75) and for bulk concentrations of 10 mM, 100 mM, and 1 M. Additional charge densities (0.22, 0.66, 1.32) are included for 1 M. The agreement between MD and c-DFT is judged as excellent for 1 M but degrades moderately at the lower concentrations. MD results are not included for 1mM due to the statistical difficulty in obtaining convergence of the very low ion densities in the channel center.

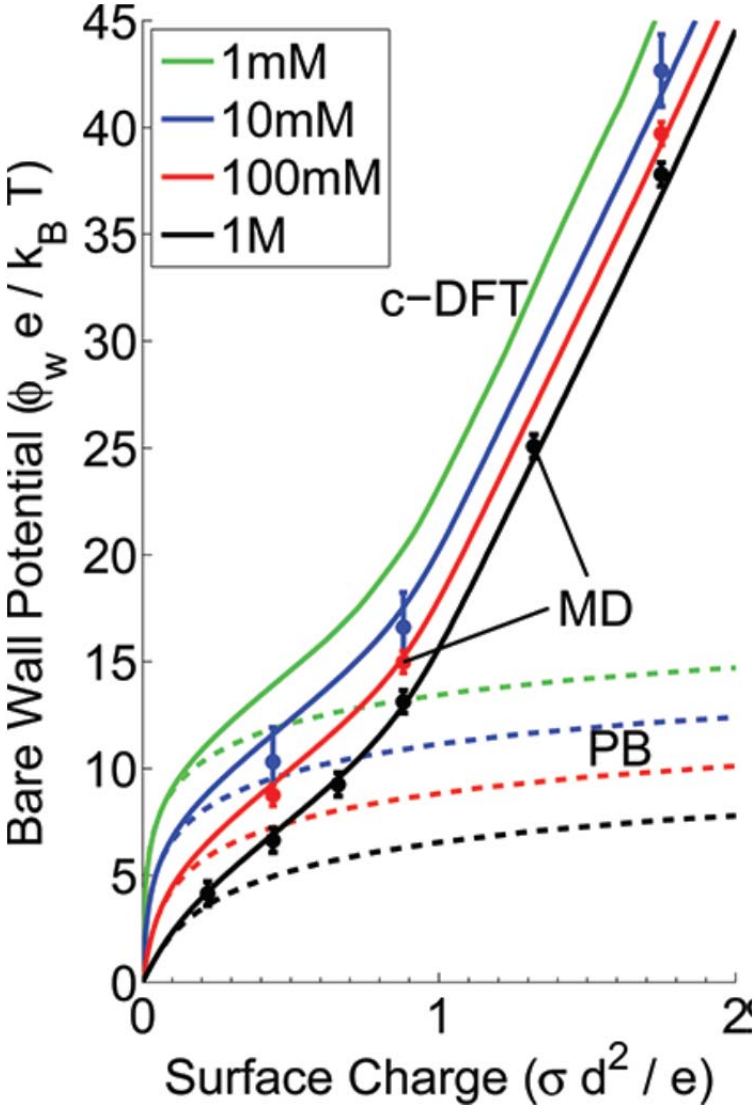

Figure 1. Capacitance comparison of three EDL models. MD is shown with circle markers and error bars which denote the standard deviation of the data set. c-DFT is shown with solid lines, and PB is shown with dashed lines. Colors denote bulk ion molarities, as shown in the legend.

2.3. Sequential Layer Charging Phenomenology

Charging of the EDL proceeds largely as a sequential layer-by-layer displacement of solvent molecules by counterions, as illustrated in Figure 2 with c-DFT results at 10 mM. Similar results were observed in the MD, particularly at higher concentrations. As seen in the inset density profiles for $\sigma^* = 1.0$, all of the solvent has been displaced from the first layer prior to the formation of a second layer of counterions. With increasing surface charge density, the counterion density peaks in the first and second layers both continue to increase in height and narrow in width until all of the solvent has been excluded from the second layer, as seen in the inset for $\sigma^* = 2.1$. The third stage of the process continues in a similar fashion until all of the solvent has been displaced from the third layer at $\sigma^* = 3.6$.

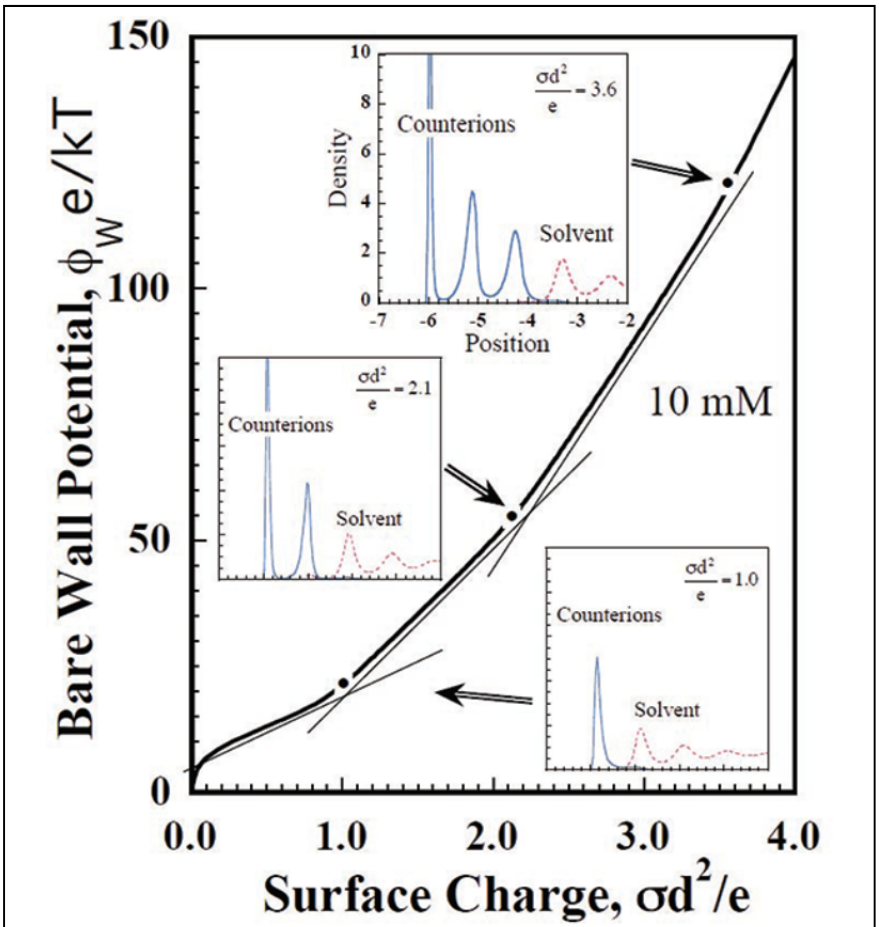

Figure 2. Layer filling phenomenology.
Aside from initial nonlinear behavior, the capacitance trend is a nearly piecewise linear function. Inflection points correspond to solvent depletion from subsequent near-wall layers, as depicted in the figure insets.

Another interesting feature of this step-like layer filling process is that each stage proceeds with a nearly constant capacitance, as indicated by a constant slope in Figure 2. The transition from one stage to the next is smooth but most of the charging occurs as a piecewise linear process with the slope increasing (and the capacitance decreasing) with each successive stage. This seems physically reasonable, as it becomes more difficult to accumulate charge in layers more remote from the surface. However, this interpretation does not appear to apply in the initial charging of the first layer, which begins with a very steep slope (small capacitance) before turning off onto a much flatter, nearly constant slope. The initial nonlinear phase occurs because ionic charges are relatively evenly distributed through the EDL for low surface charges. As loading increases, peak formation becomes energetically favorable, and most of the charge is found distributed near the walls. As the peak builds up (likewise for subsequent layers), the peak structure's contributions begin to dominate those of the tail. Aside from the initial nonlinear phase, these features of the charging behavior are expressly absent from theories not accounting for finite size effects since the physics arise from layered density profiles and solvent displacement processes entirely foreign to PB.

The simulations performed in this study used the 3CM, in which solvent and solute are represented by three distinct molecular species. The fluid−fluid and fluid−solid interactions use LJ-type potentials, in contrast to previous c-DFT-to-MC comparison studies, which utilized hard-sphere and hard-wall repulsions. In further contrast with previous studies, our simulations cover a wide range of electrolyte concentrations and surface charge densities. Our MD models are able to simulate concentrations as low as 10 mM and still produce density profiles in agreement with c-DFT over a five to six decade range. All of our nanochannels are sufficiently wide to prevent overlapping EDLs, even in the case of low ion concentrations (hence large Debye lengths). A discernible bulk region with zero potential is important for direct comparison between MD and c-DFT.

As a result, MD and c-DFT methods are in excellent agreement for various qualitative and quantitative assessments, particularly for large molarities. Metrics for assessment include atomic density, charge density, electric field, and electric potential profiles, as well as capacitance trends for various loadings and concentrations. Specifically, density profiles agreed particularly well on

peak location and spacing, while differing slightly on peak height and width. Comparisons are improved when c-DFT uses a modified hard sphere radius of $d_{hs} = 0.93d_{LJ}$ and the MSA_L implementation. MD calculations tended to have taller, narrower peaks than the c-DFT; this is resolved by the fact that there is an equivalent amount of charge in the layer. Moreover, as electrolyte concentration decreases and surface charge loading increases, deviation from PB becomes increasingly apparent. These trends highlight the effect of distinct ion packing layers, which is due to the finite sizes of electrolyte and solute. Distinct layers result in significantly reduced capacitances relative to the predictions from PB theory. Further investigation shows a layer packing phenomenon in which a new ion peak begins to form when solvent is completely expelled from the previous fluid layer. The onset of the new ion peak produces a kink in the electric field and electric potential profiles, thereby reducing the capacitance of the EDL. Since this behavior arises from finite size effects, it is not captured in PB theory.

2.4. Conclusions

This work is a step toward modeling more complex systems. As mentioned previously, we will be exploring complex EOF models with polar solvents and atomistically structured walls including surface roughness. We are exploring the plausibility of modeling structured walls with higher dimensional c-DFT to study surface effects such as packing structures. Additionally, by modeling representative unit cells with 3D c-DFT and linking them with continuum-like boundary conditions, we can study large-scale surface roughness.

3. COMPARISON OF MOLECULAR AND PRIMITIVE SOLVENT MODELS FOR ELECTRICAL DOUBLE LAYERS IN NANOCHANNELS

This section contains highlights of a publication. For details see Lee, J. W.; Templeton, J. A.; Mandadapu, K. K.; Zimmerman, J. A.; "*Comparison of Molecular and Primitive Solvent Models for Electrical Double Layers in Nanochannels,"* J. Chem. Theory Comput. *9*, **2013**, 3051−3061.

3.1. Introduction

In the work described in the previous section, it was shown that an electrolyte solution can be modeled in molecular dynamics (MD) simulations using a uniform dielectric constant in place of a polar solvent to validate Fluid Density Functional Theory (f-DFT) simulations. This technique can be viewed as a coarse-grained approximation of the polar solvent and reduces computational cost by an order of magnitude. However, the consequences of replacing the polar solvent with an effective permittivity are not well characterized, despite its common usage in f-DFT, Monte Carlo simulation, and Poisson−Boltzmann theory. In the work described below, we have examined two solvent models of different fidelities with MD simulation of nanochannels. We find that the models produce qualitatively similar ion density profiles, but physical quantities such as electric field, electric potential, and capacitance differ by over an order of magnitude. In all cases, the bulk is explicitly modeled so that surface properties can be evaluated relative to a reference state. Moreover, quantities that define the reference state, such as bulk ion density, bulk solvent density, applied electric field, and temperature, are measurable, so cases with the same thermodynamic state can be compared. Insights into the solvent arrangement, most of which cannot be determined from the coarse-grained model, are drawn from the model with an explicitly described polar solvent.

Characterizing the behavior of an electrolyte fluid confined between solid surfaces is important for research and technologies ranging from energy storage[1,18,19] to microfluidics based biology.[20,21] According to classical theories, ions near a charged wall form an electric double layer (EDL),[22] which is comprised of the Stern layer, a mostly immobile layer of counterions closest to the wall, and the diffuse layer, a region of decaying electric potential where both

counterion and coion species can be present. The characteristic length scale of the EDL is referred to as the Debye length:

$$\lambda_D = \sqrt{\frac{\varepsilon k_B T}{2n^0 e^2}}$$

where k_B is the Boltzmann constant, T is the temperature, n^o is the bulk molarity, and e is the elementary charge. The permittivity of the medium, ε, is the product of the vacuum permittivity, ε_o, and the relative permittivity, ε_r. It has been shown that as the Debye length approaches molecular length scales, the Classical Poisson−Boltzmann (PB) theory breaks down.[23,24] The continuum-based PB theory has been widely used in the modeling of electro-osmotic flow (EOF), electrochemical capacitors, etc.[3,4,7,25-28] While the theory is a reasonable approximation for low ion concentrations and low surface charges, finite particle sizes and atomic packing structures lead to inaccuracy.

In PB theory, ions pack near the wall according to the Boltzmann distribution with the corresponding surface potential. Ions are assumed to be infinitesimal in size, and particle interactions are assumed negligible. The first order approximation of the Boltzmann distribution is expressed as

$$n_+ = n_+^0 \, exp\left(\frac{-\phi e}{k_B T}\right)$$

and

$$n_- = n_-^0 \, exp\left(\frac{\phi e}{k_B T}\right)$$

where n is the molarity of the ion species, ϕ is the local value of the total electric potential (relative to the bulk value), and subscripts denote the sign of the ion charge. Note the distribution dictates that the counterion concentration decays monotonically away from the surface. However, in the case of atomistic simulations, atoms and ions will form a particular packing structure, which yields peaks and valleys in their density profiles.[24] As electrolyte concentrations and applied voltages increase, resolution of the density oscillations becomes increasingly important. In this regime, engineering based on PB theory becomes unfeasible. It

should be noted that modified PB theories have been proposed which correct for finite packing.[29-34] While these provide density distributions that are much more physically reasonable, we will be exploring options that give a more explicit description of the equilibrium EDL state to gain a better understanding of atomistic and molecular effects.

To that end, simulation techniques such as Fluid Density Functional Theory (f-DFT), Monte Carlo (MC), and molecular dynamics (MD) may be used to elucidate double layer physics. For example, f-DFT has been utilized to calculate over a wide range of surface potentials and ionic concentrations.[14,23,24] The work of Tang et al.[14] in the early 1990s modeled 0.1 molar (M) and 1 M solutions with normalized surface charges ranging from 0.05 to 0.7. Nilson et al.[23] expanded on this work while studying EOF in nanochannels with simulations ranging from 1 mM to 1 M for normalized surface charges from 0.0 to 1.0. The advantage of these f-DFT calculations is that reference state properties (i.e., reference energy, bulk fluid density, and bulk ionic concentration) are all specified as boundary conditions. However, f-DFT has theoretical and numerical difficulties simulating bonded molecules with angle constraints. As such, to our knowledge, there is no evidence of published f-DFT work using the molecular solvent model (MSM), where atomic constituents of each solvent molecule and solute ions are explicitly described as distinct atoms. Henderson et al.[35] used a symmetric dumbbell solvent model in f-DFT to approximate the effects of polar water. Alternatively, f-DFT has typically utilized the primitive model (PM),[36] the restricted primitive model (RPM),[13] and the three-component model (3CM)[14] in simulating such systems. PM describes the solvent material as a uniform, isotropic dielectric continuum, and therefore, it is not explicitly modeled. The RPM additionally restricts PM such that the two ionic species are the same size. The 3CM, a coarse-grained approximation of the MSM, simulates the solvent molecule as a charge-neutral atom. Typically, ions are also restricted in size as with RPM. It is with the 3CM technique that PB theory can clearly be shown to deviate from atomistic results.[23,24] The 3CM has been used with f-DFT and MD to show deviations from PB theory at higher surface charges.[23,24] However, the assumption of a uniform dielectric constant in the 3CM is potentially problematic close to the surface. While MD studies of electrolyte solutions near electrified interfaces have been performed using both the 3CM[8,24] and MSM,[3-7,10,24,37−40] the consequence of the 3CM approximation has not been quantified. In the work discussed here, the 3CM is compared against the higher fidelity MSM using various metrics,

such as capacitance, spatial variations in density, electric field, and electric potential, and near-wall fluid structure. While the ionic density profiles show some qualitative agreement, closer inspection shows major discrepancies in surface properties relative to the reference state. We will also show that, even for low surface charges, the MSM produces results that cannot be reproduced by the 3CM.

3.2. Results

An overview of the model comparison is presented in Figure 3. It shows computed electric surface potentials for the negative and positive walls as a function of the applied surface charge for a nominal molarity of 1 M. Both the 3CM and the MSM are overlaid on top of each other for comparison purposes. The inverse of this curve is typically used to find the capacitance of the double layer by taking its slope (specifically the capacitance of the material between the measurement location and the reference).

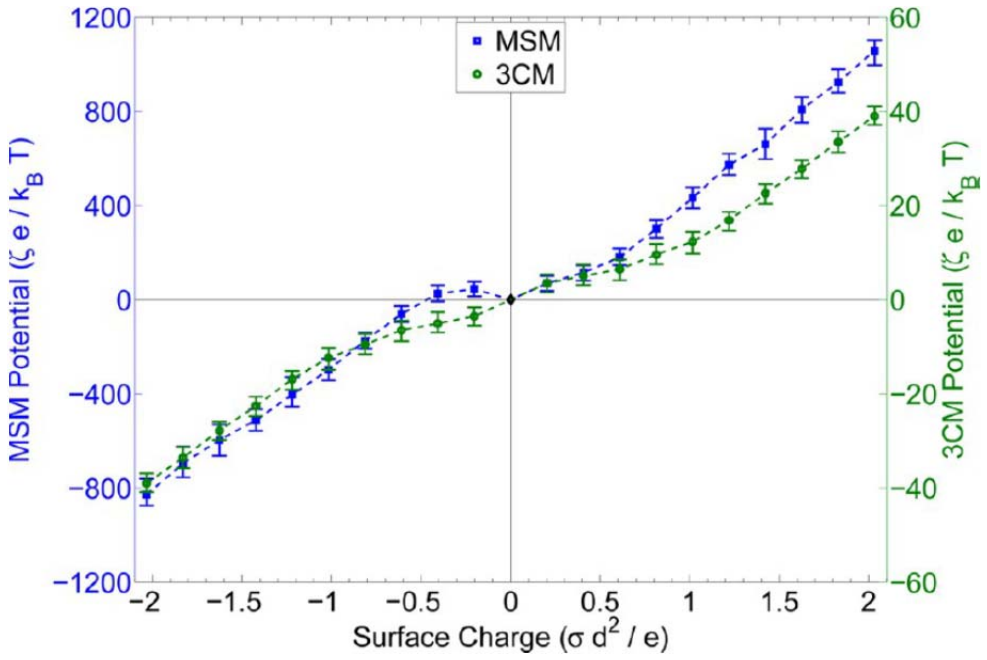

Figure 3. Electric potential relative to the bulk as a function of surface charge for the 3CM and MSM.
The MSM results are plotted with blue squares on the left axis, and the 3CM results are plotted with green circles on the right axis. Minimum and maximum potentials observed in the course of the MD simulations are denoted by the error bars to estimate the uncertainty in those measurements. The inverse of the slope is the capacitance of the EDL. The 3CM is intrinsically symmetrical, but the MSM curve shows clear asymmetries.

Here, the electric surface potential is defined to be the electric potential measured at the fluid-wall interface, relative to a specified reference location, which we have chosen as our bulk fluid. It will be pointed out later that our bulk is a good choice for the reference potential. The asymmetry of the MSM solvent creates an asymmetric surface potential trend, which cannot be reproduced by the 3CM. Ironically, for low, negative surface charges, the MSM yields a positive potential. This is due to a number of factors, including but not limited to (i) the choice of measurement plane, (ii) the short distance between the wall and hydrogen atoms (from adsorbed water molecules), (iii) the small slope of the electric potential, and (iv) the relatively large amount of water molecules (compared to adsorbed counterions), which causes the hydrogen atoms to locally overscreen the applied electric field. Given that the inverse of the ζ versus σ curve is not a proper function, one should be cautioned when attempting to measure a capacitance. While the applied surface charge is the same for both models, potentials are plotted on different scales because the electrostatic interactions are between 1 and 2 orders of magnitude different. In general, these results are in agreement with earlier theoretical and computational studies, which have shown that capacitances measured from primitive models (e.g., 3CM) can be greatly overpredicted due to mischaracterization of the dielectric response near interfaces.[41] The difference in magnitude of electric surface potential for the two models will be discussed in detail later.

3.2.1. Density Profiles

Figure 4 shows the density profiles for the 3CM cases on a linear scale. Due to the antisymmetry of the model, only one wall is shown. The zero x-axis position in subsequent profile plots indicates the origin of the LJ wall. For discussion sake, we will label the cases 1 to 10, starting from the lowest surface charge case (consistent with axes labels in the figures). In accordance with observations by Lee et al.,[24] formation of the second counterion peak coincides with depletion of the solvent in the first peak position. Also, as surface charge increases, the ion peak shifts moderately toward the wall because surface repulsion is a soft-core interaction.

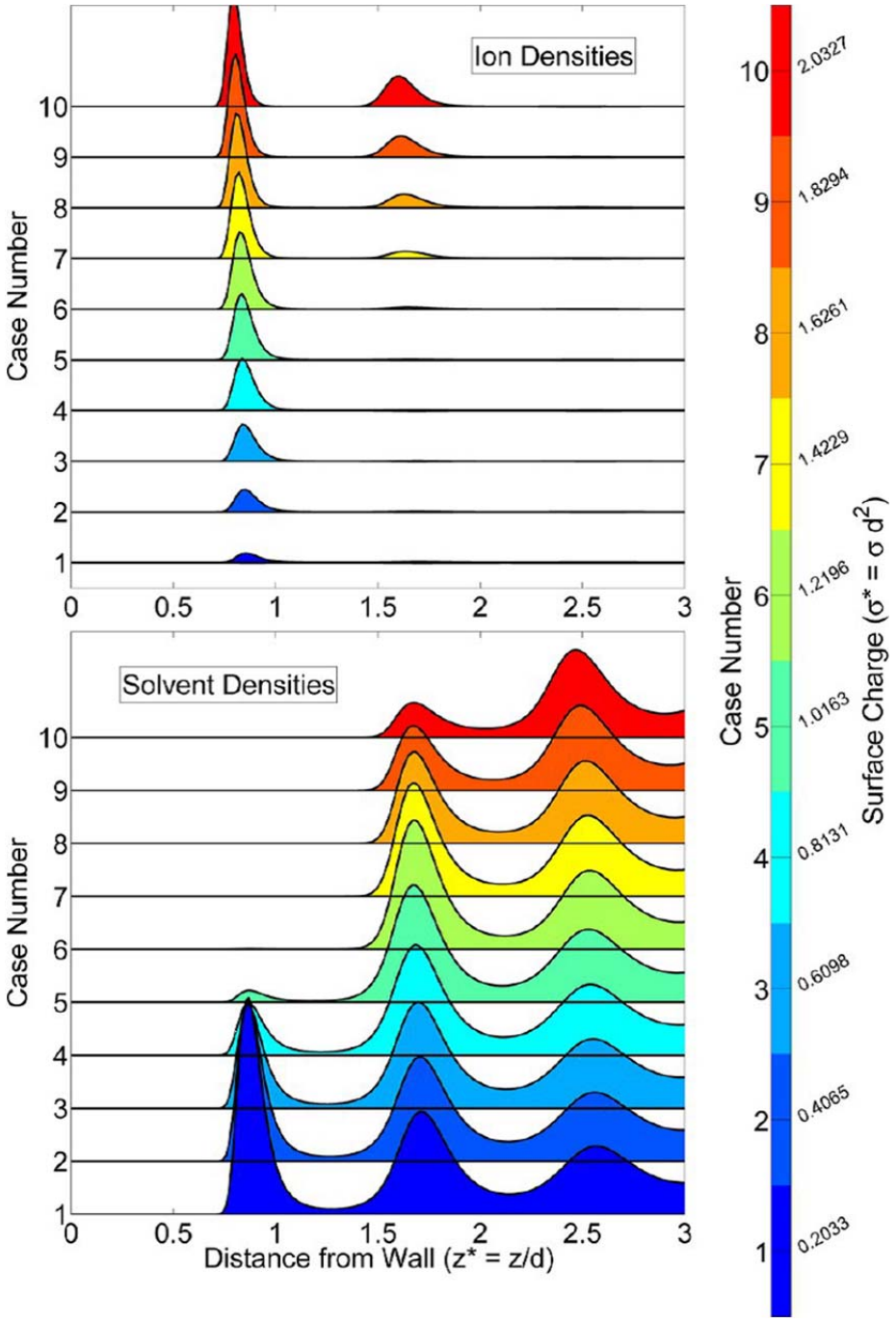

Figure 4. 3CM density profiles at 1 M and various surface charges.
The upper plot is for the ion density, and the lower plot is for the solvent density. For the ion densities here, counterion densities are plotted as positive values, and coion densities are plotted as negative values. Each surface charge case is plotted at a different offset for comparison purposes.

Figures 5 and 6 show the density for the MSM results, both on a linear scale. Here, the left and right surfaces are plotted independently because of the asymmetry. Solvent density is split into two plots for the hydrogen and oxygen components.

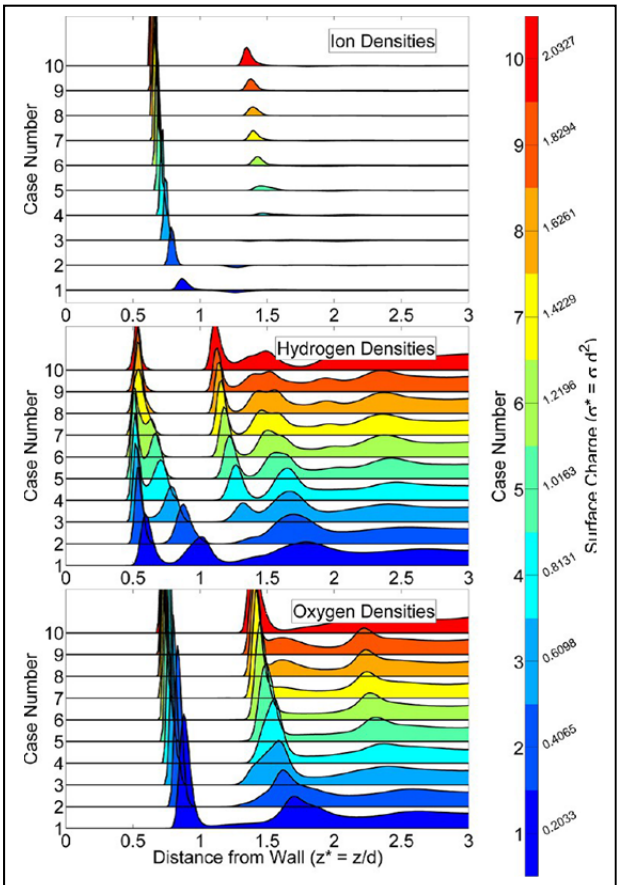

Figure 5. MSM density profiles at 1 M and various negative surface charges. For the ion densities here, counterion densities are plotted as positive values and coion densities are plotted as negative values. Each surface charge case is plotted at a different offset for comparison purposes.

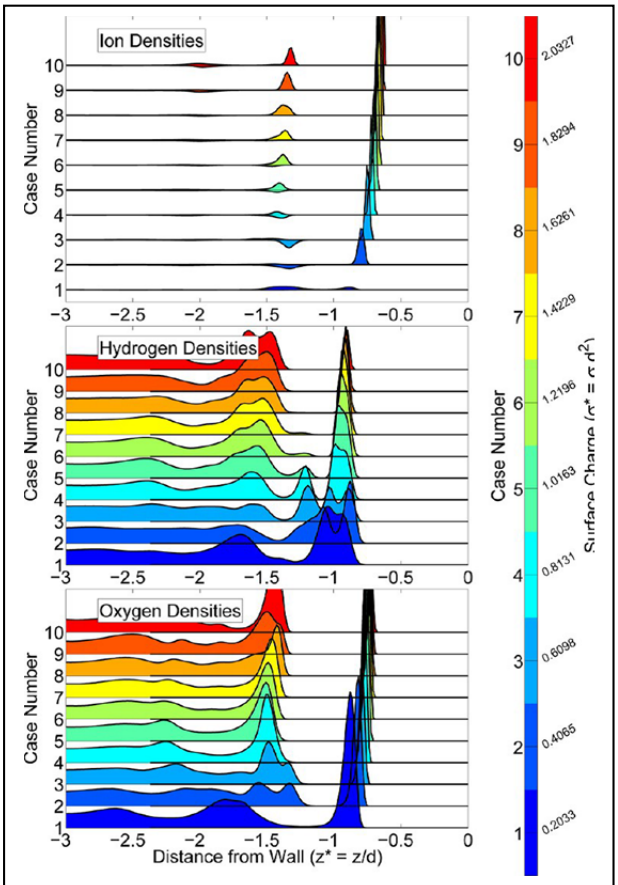

Figure 6. MSM density profiles at 1 M and various positive surface charges. For the ion densities here, counterion densities are plotted as positive values and coion densities are plotted as negative values. Each surface charge case is plotted at a different offset for comparison purposes.

In the MSM, ions also shift closer to the surface as surface charge increases, but much more noticeably than in the 3CM case. It appears to have asymptoted to its limit in the highest surface charge case. The decreased distance to the wall is magnified in the MSM case, at least in part due to the increased electrostatic interactions; recall that the 3CM interactions are weakened by a factor of 80, whereas the MSM interactions are only effectively weakened in the presence of solvation shells. With the MSM, not only does the wall partially disrupt solvation shells but also

solvent near the wall has the tendency to align with the applied field rather than solvating nearby ions. Moreover, within the double layer, polarizability of the solvent is not necessarily equivalent to a relative permittivity value of 80, as this number applies specifically to bulk water.[42,43] Interestingly, as ions shift toward the surface, solvent also shifts with them; this phenomenon is not observed in the 3CM. It is perhaps due to the electrostatic interactions between the surface and the solvent being present in the MSM but not the 3CM. Also interesting is that complete solvent depletion is not observed in these MSM simulations, despite formation of the second ion layer. Solvent behavior is particularly interesting. For negatively charged surfaces (Figure 5), the alignment of the water molecule shifts significantly as surface charge is increased. Strictly looking at the first layer of atoms, the dipoles from the low surface charge curves are only slightly oriented toward the surface. This can be seen from the first two hydrogen peaks (asymmetrically) straddling the first oxygen peak. By the highest surface charge, the hydrogen peaks have consolidated into one, which suggests the dipole vector is pointing directly toward the wall.

On the other hand, Figure 6 shows that the positively charged surface behaves differently. The first two or three cases show a very slightly off-axis dipole vector, but otherwise, the water molecule maintains approximately the same orientation for all surface charges. Curiously, only a few intermediate surface charge cases (i.e., cases 2−4) show a straddled water molecule in the second layer, but this feature is not observed in the second layer for higher or lower surface charges.

3.3. Conclusions

To better understand the EDL and the physics that affect it, we compared two different solvent models using MD simulation. The MSM explicitly models the atoms in the polar molecule (in this case, TIP3P water). On the other hand, the 3CM can be viewed as a coarse-grained approximation where the solvent is treated as a chargeless atom, and a uniform dielectric constant is used to account for the polar nature of solvating fluids. It was shown that the 3CM and the MSM produce ion densities that are qualitatively similar, but close inspection reveals

subtle differences in positions. These subtle differences and details about the orientation of solvent molecules for the MSM greatly affect the quantitative measurements of electric fields, electric potentials, and capacitances. Near the wall, these quantities are shown to differ by an order of magnitude. Moreover, the MSM allows a larger amount of coions to exist in the EDL, to the point of exceeding counterion densities in some regions. This has not been observed in any 3CM study (past or present) or PB theory. Due to this phenomenon and other complex effects in the MSM, the electric field and electric potential are observed to overshoot the requisite screening, and decaying oscillations bring them to bulk conditions. Density, electric field, and electric potential patterns are observed in the 3CM to repeat from one layer to the next for different surface charge cases. This happens when the first ionic layer screens away enough electric field to match the applied electric field of a lower surface charge case. Also in the 3CM, the residual electric field between the first and second layers linearly increases with the applied charge. However, in the MSM, repetitions do not occur linearly nor do they advance in an equivalent manner as the applied charge increases. Moreover, these repetitions are observed only at the negatively charged surface. We also calculated correlation function contour plots that reveal water molecule reorientation effects and oscillations of coion and counterion charge. The reorientation of water indicates that the water's tendency to solvate ions near the wall is effectively nullified under high surface charges, thus having the direct consequence of altering the permittivity.

4. ATOMISTIC EFFECTS IN ELECTRIC DOUBLE LAYERS AT HIGH VOLTAGES

This section contains highlights of a publication. For details see Lee, J. W.; Mani, A.; Templeton, J. A.; "*Atomistic Effects in Electric Double Layers at High Voltages,"* Langmuir, submitted, **2013**.

4.1. Introduction

The Poisson-Boltzmann theory for electrolytes near an electrified surface is known to be invalid in the high charge limit due to unphysically large ion concentrations near the surface. To investigate this regime, fluids density functional theory (f-DFT) and molecular dynamics (MD) simulations, were used to determine electric surface potential as a function of surface charge. Based on these detailed computations, we present a remarkably simple model, which accurately predicts the surface charge capacitance at high charges. The model contains no tuning parameters and compares well with our f-DFT and MD results by incorporating atomistic effects. Deviations are only observed in the low charge regime, where Poisson-Boltzmann effects are more pronounced. The simplicity of the model illuminates the important factors that govern the double layer in the high charge limit, namely the applied surface charge and ionic packing fraction.

With the increased interest in electrical energy storage, research on the interface between electrolytes and electrified substrates has increased. Various theories for the electric double layer (EDL) have been developed and studied, most notably mean- field theories such as Poisson-Boltzmann/Gouy-Chapman theory and subsequent modifications to include steric effects.[29-34,44-47] The original Gouy-Chapman model assumes a Boltzmann distribution of ions sufficient to screen the surface charge, with a characteristic length scale referred to as the Debye length. This model allows for unlimited ion concentrations near the solid-fluid interface, surpassing physically allowable close packing density for surface charge magnitudes common to microfluidic pumps, electrochemical sensors, and supercapacitors. In general, the permittivity varies depending on the local medium, i.e. $\varepsilon = \varepsilon_r\varepsilon_0$, where ε_r is the medium's relative permittivity, and ε_0 is the vacuum permittivity. The main assumptions of most Gouy-Chapman-type models are (i) ε is constant, and (ii) the only significant interactions are Coulombic.[44-46] A third

assumption (which is implied by the two but worth noting) is that the solvent does not affect the equilibrium configuration of the system, aside from providing a dielectric medium.

Typical modifications to the Gouy-Chapman theory involve statistical mechanical derivations to include a Stern layer[46] immediately adjacent to the surface. Borukhov *et al.*,[32] for example, presented a modified Poisson-Boltzmann (MPB) theory which prevents ion concentrations from exceeding $1/d^3$, where d is the ion diameter. In the high charge limit, the model predicts an electric surface potential of

$$\frac{\varsigma e}{k_B T} = \frac{1}{2}\frac{d^3\sigma^2}{\epsilon k_B T}$$

where σ is the surface charge density. Typical surface charges may vary depending on electrode material, but they are normally bounded by O(1) C/m^2.

Kilic et al.[47] developed a composite diffuse layer (CDL) model assuming a “condensed layer" in place of the Stern layer. The condensed layer is a continuum region of counter-ions with uniform density (co-ions are excluded from the condensed layer). At the interface between the condensed layer and the outer diffuse layer, the electric field is used for boundary condition matching. The CDL model simplified for the high charge limit yields the same behavior as the MPB model. To our knowledge, these models have not been quantitatively verified at the high charge limit against experiments or a high fidelity numerical simulation.

4.2. Results

In this work, we use fluids density functional theory (f-DFT) and molecular dynamics (MD) simulations to rigorously investigate the charge-potential relations without resorting to a macroscopic model. We are exploring the upper limit on surface charge density and its effect on ionic packing and capacitance. Our results show the details of the precise close-packing arrangement in such a limit, which yields a simple and idealized model that can capture the charging dynamics of the EDL while accounting for deviations from continuum theories caused by the discrete nature of the atoms.

Here, we propose a simplified model, by focusing only on the packing effects and neglecting all other physics associated with steric effects and the diffuse layer. We assume that in the limit of large surface charge, the potential drop in the EDL is governed by a region of densely packed multi-layered counter-ions, i.e. a condensed layer. Figure 7 shows example snapshots from our MD simulations. The cross-sectional view (Figure 7b) reveals a triangular packing arrangement, which we infer to be to a hexagonal close-packed or face-centered cubic lattice. Both lattices yield the maximum packing fraction of 0.74. The thickness of this condensed layer is assumed to be such that the total charge balances the applied surface charge. In this model, we simply ignore contributions of the diffuse layer to the potential drop. As we shall see, this approximation is valid since the diffuse layer can at most contribute potential drops on the order of a few thermal voltages, which is negligible compared to the potential across the condensed layer.

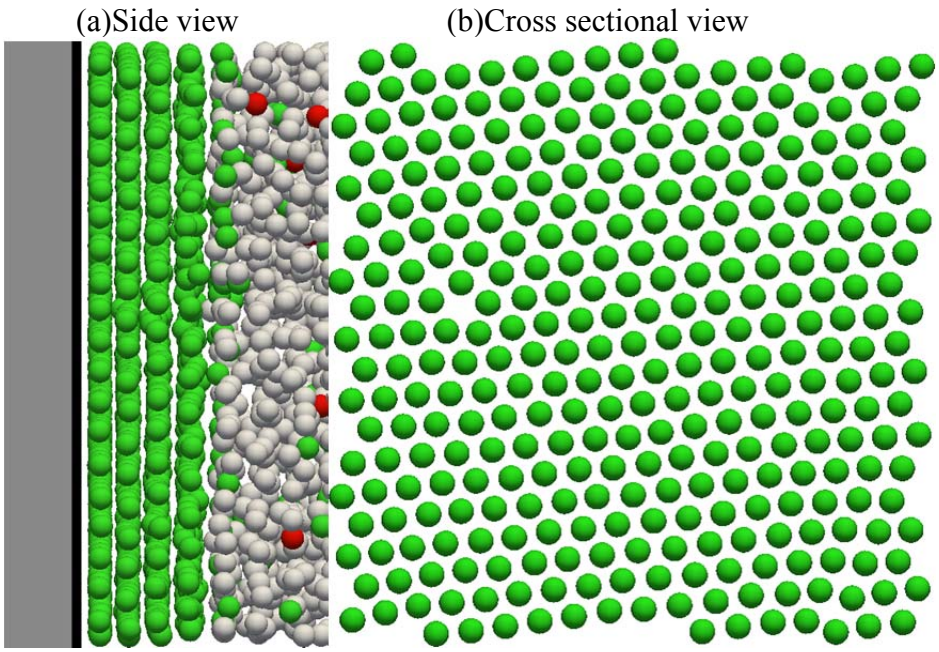

Figure 7. Snapshots from our MD simulations.
(a) A side view of ionic packing arrangement. (b) A cross-sectional view of one ionic layer near the surface.

It should be noted that strong oscillations near the walls are observed in the density profiles from both types of simulation. These lead to step-like functions in the electric field plots and inflection points in the electric potential plots. Those inflection points correspond to inflection points in the charging curve. As shown in Lee et al.,[24] the capacitance in between each of those inflection

points is approximately constant. Conversely, our theoretical model assumes that the counter-ion density in the near-wall region is a uniformly distributed block of charge. Despite this simplification, the capacitance is still observed to follow the same trend and be quantitatively well predicted because we identify the most important atomistic effect, namely packing density, and incorporate it into the model. This indicates that in the high charge regime, density oscillations arising from atomic packing are not particularly important. In other words, for the high surface charge regime, the inflection points in the capacitance trend appear so closely spaced that the curve is essentially quadratic. Also negligible is the diffuse layer and its contribution to screening the surface.

4.3. Conclusions

By understanding which effects dominate double layer capacitance and which are less relevant, it is possible to extend the theory to other electrolytes by estimating their packing structure and distribution of co-ions, counter-ions, and solvent molecules in the condensed layer. In identifying the degree to which atom packing influences double layer physics, this work demonstrates that, contrary to other EDL theories, the specific electrolyte and arrangement of surface atoms will be critically important to predict its electrical properties through their impact on ion packing. The proposed model offers a simple and straightforward means to incorporate these effects in assessing double layer capacitance. Future efforts will systematically consider deviations from spherical shaped molecules through the maximum packing factor and incorporate changes to the electric medium near the surface.

In summary, we used f-DFT and MD simulations to numerically determine the charge-potential relationship in the high charge regime. Given a close-packed arrangement of ions near the surface, we proposed a simple theoretical model for the EDL in this limit. We model the charge density near the wall as a uniform block of charge sufficient to entirely screen the applied surface charge. The simulations and theoretical model both predict a quadratic dependence of potential on surface charge density, consistent with earlier models. Moreover, the maximum packing density and hard-sphere diameter played significant roles in achieving the remarkable agreement between simulations and model. Notably, our model does not need any tuning parameters. It takes only three physical parameters: (i) the dielectric constant of the condensed layer, (ii) hard

sphere packing fraction of the condensed layer (confirmed to be HCP and/or FCC from MD simulation), and (iii) hard sphere diameter of the ions. As such, the model can be easily adjusted for cases where the solid substrate dictates the lattice arrangement of ions. Density oscillations commonly observed near solid surfaces and Poisson-Boltzmann effects are shown to be of little consequence in this regime. Thus, the model shows an insensitivity towards permittivity in the bulk. It remains to be seen how accurate the model's predictions are for more complicated electrolytes.

5. EXPERIMENTAL BACKGROUND

The experimental goals of this project were to develop optical spectroscopic capabilities that can probe electrochemical interfaces to determine molecular species present, molecular orientation and electric fields. Our work has focused on development of interfacial molecular vibrational spectroscopies and nonlinear optical spectroscopy that is sensitive to the electrical properties of the interface. An important aspect of this portion of the project was the development and characterization of electrified interfaces suitable for optical probing and accessible to theoretical modeling. We have grown single crystal gold plates that are optically transparent and electrically contacted to conductive indium tin oxide surfaces for studies at crystalline gold interfaces. Several self-assembled monolayer (SAM) surfaces on gold substrates have also been developed including SAMs functionalized with Stark-shift electric field probes such as small molecules with strong dipole moments. In particular, alkane thiols functionalized with cyano groups have been synthesized and incorporated into alkane thiol SAMs. These interfaces have been characterized with sensitive surface vibration spectroscopy using polarization modulated reflection absorption infrared spectroscopy (PM-RAIRS) implemented in this project. Using this capability we have measured the cyano group absorption spectrum at less than 10% of a monolayer surface coverage on a gold surface. We have also developed a highly sensitive confocal Raman microscope with a transmission grating spectrometer for surface vibrational spectroscopy. Graphene has recently become a prominent candidate as a high discharge rate electrode for supercapacitors. Its relatively simply structure also makes it amenable to detailed modeling. With our Raman microscope we have measured Raman spectra of single layer graphene and recently investigated changes in its Raman spectrum with applied voltage in an electrochemical cell. Using a recently available amplified femtosecond laser we have also implemented second harmonic generation (SHG) for sensitive interfacial spectroscopy. With broadband femtosecond excitation we have measured the spectrum of SHG and determined its intensity dependence versus voltage in an electrochemical cell. With the development of these experimental approaches we have versatile capabilities for optically probing electrochemical interfaces.

6. DEVELOPMENT OF MODEL ELECTROCHEMICAL INTERFACES

6.1. Gold microplates

For direct comparison of detailed modeling with experimental results measurements on a single crystal inert substrate are ideal. An optically transparent substrate is desirable for maximum flexibility in optical probing. Using a previously described method,[48] we produced micron sized gold single crystal plates that are electrically contacted to an indium tin oxide surface. The gold particles were characterized with electron microscopy as shown in Figure 8.

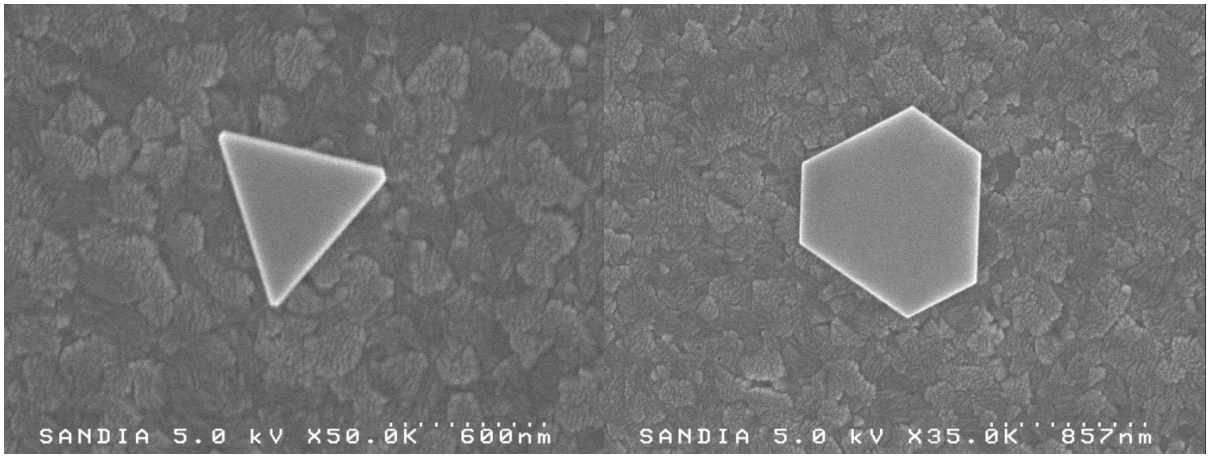

Figure 8. Electron micrographs of single crystal gold microplates on indium tin oxide. Single crystal gold is an ideal model interface. Transparent, electrically contacted gold microplates give maximum flexibility for optical diagnostics. The microplates are ~20 nm thick.

The gold microplates were functionalized with mercaptobenzoic acid to measure their activity as surface enhanced Raman substrates. Raman spectra of mercaptobenzoic acid were measured with the confocal Raman microscope described below, but we have not found that the microplates, functionalized in this way, reliably enhance the Raman spectra. Different functionalization strategies on these substrates may yield reliable surface enhancement, and the microplates are also promising for future measurements using SHG microscopy.

6.2. Self-Assembled Monolayers Characterized by PM-RAIRS

Self-assembled monolayers serve as relatively simple models of more complex electrode surfaces and their electrochemical properties have been extensively measured.[49-52] The electrical conductivity and capacitance characteristics of SAMs can be varied depending on their molecular components. We have developed several self-assembled monolayer (SAM) surfaces on gold substrates suitable for optical probing. First are simple octadecanethiol and mercaptobenzoic acid SAMs on gold coated microscope coverslips. The formation of the SAMs is verified by observing the change in water contact angle. For making electric field measurements above the SAM surface a series of alkane thiols functionalized with cyano groups have been synthesized. The vibrational transition frequency of the cyano group is expected to depend on the local electric field as a result of the vibrational Stark shift.[53] The formation of SAMs doped with cyano-alkanes has been studied using a PM-RAIRS spectrometer we have implemented. Using this capability we have measured the cyano group absorption spectrum at less than 10% of a monolayer surface coverage on a gold surface. The SAM surfaces developed are also suitable for surface enhanced Raman spectroscopy (SERS) studies with the development of a suitable substrate with reliable surface enhancement.

The PM-RAIRS spectrometer developed is based on a Bruker Tensor 27 FTIR spectrometer. The FTIR beam path is extended outside the spectrometer and focused onto the sample surface with a custom, electronically-controlled optical system. The reflected beam from the sample is focused onto an external detector. The polarization of the IR beam before the sample is modulated using a Hinds photoelastic modulator and the signal is detected with lock-in detection at the modulation frequency. Since the surface absorption on the conductive substrate strongly favors the vertical polarization the PM-RAIRS technique provide a highly surface sensitive absorption spectrum. PM-RAIRS spectra of a monolayer SAM of octadecanethiol is shown in Figure 9. Spectra of a mercaptobenzoic acid SAM and the CN region of a SAM containing 10% cyano-alkane are shown in Figure 10. Further improvement of the PM-RAIRS operation and careful electrochemical cell design should enable absorption spectra of *in situ* interfaces.

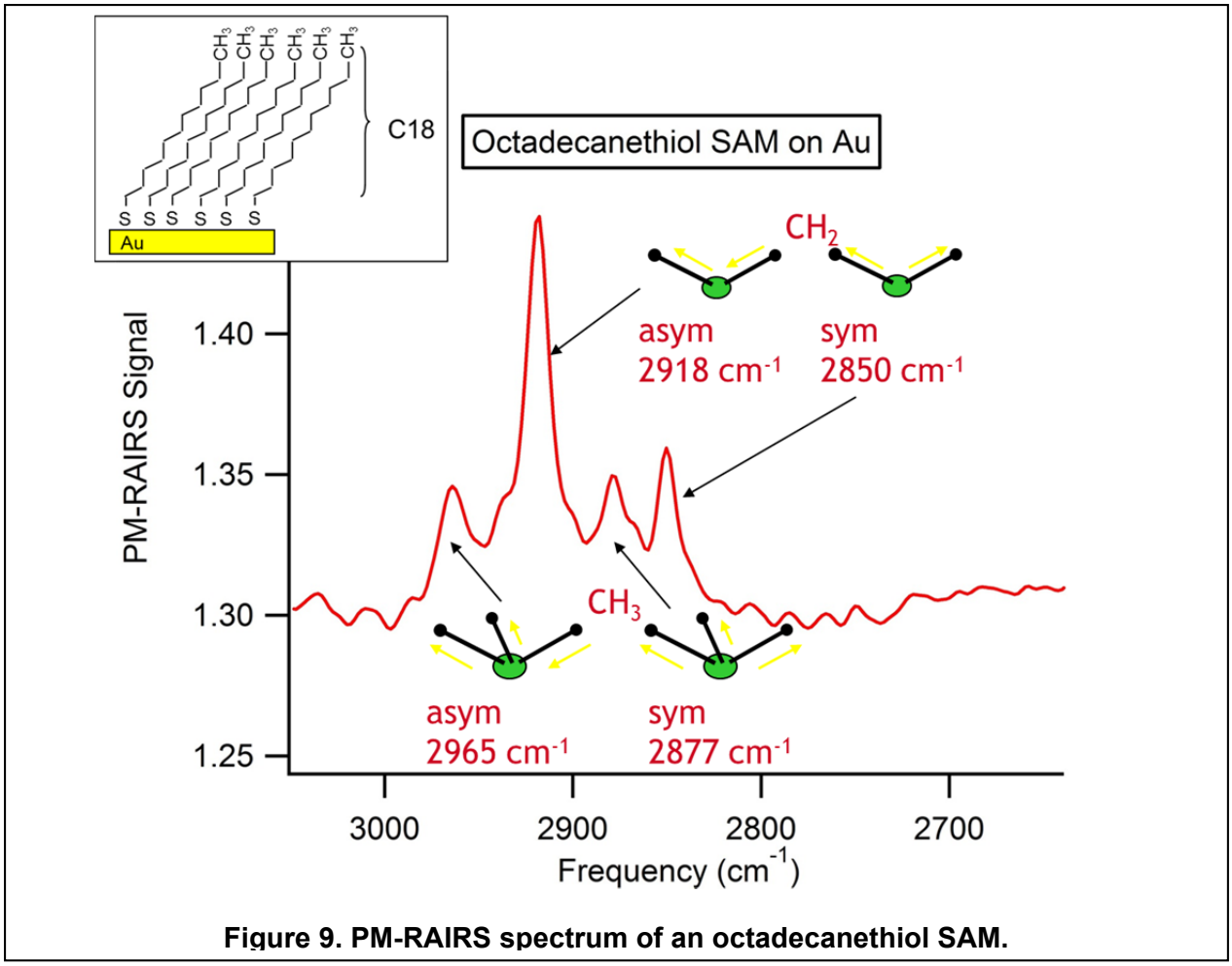

Figure 9. PM-RAIRS spectrum of an octadecanethiol SAM.

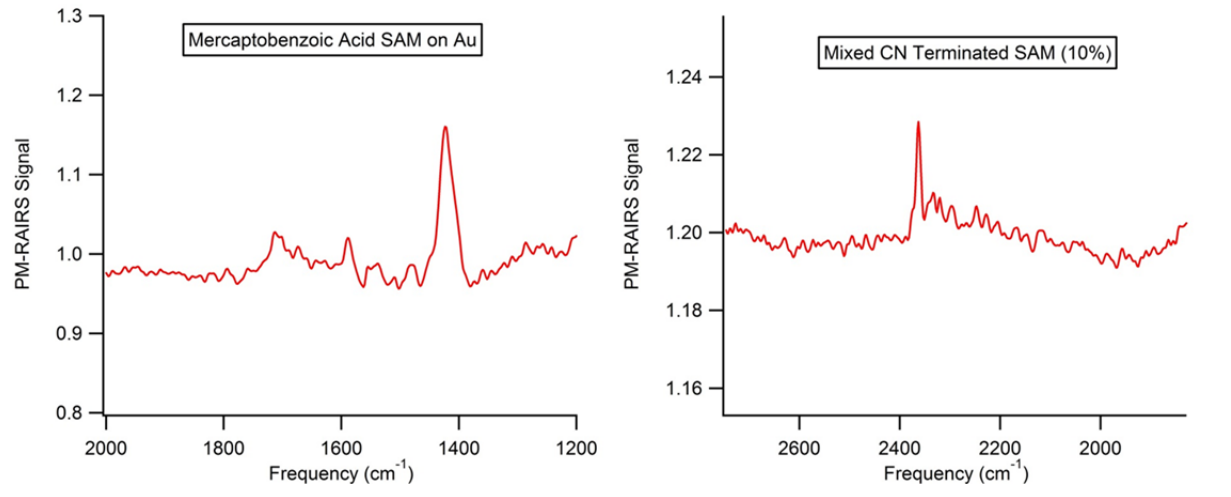

Figure 10. PM-RAIRS spectra of mercaptobenzoic acid and cyano-alkane SAMs.

7. CONFOCAL RAMAN MICROSCOPE AND RAMAN MEASUREMENTS ON GRAPHENE

Raman spectroscopy is one of the most generally useful species sensitive optical spectroscopies. Most molecular species have characteristic Raman spectra so no labels are required to selectively probe the composition of a sample. The drawback of Raman spectroscopy is that in the absence of enhancement the signals are very weak. We have developed a very sensitive confocal Raman microscope, based on an inverted Olympus IX71 microscope and a custom transmission grating spectrometer. The excitation source is fiber coupled and thus any available laser source can be readily used. The excitation laser is directed through the microscope objective and focused onto the sample. The backscattered Raman signal is collected by the objective and is focused through a confocal pinhole then collimated onto the transmission grating. The transmission grating (Wasatch Photonics) has greater than 80% diffraction efficiency throughout most of the visible wavelength range of interest, and importantly is nearly polarization insensitive so both polarizations are detected with equal sensitivity. The dispersed signal light is focused onto a cooled CCD camera. Custom software reads out the lines on the camera containing the spectrum and synchronizes the camera readout with the scanning of a precision piezoelectric stage that scans the sample to create a spectrally resolved image.

Graphene is a one-atom thick layer of crystalline carbon with carbon atoms arranged in a regular hexagonal pattern.[54] Graphene has very desirable characteristics for carbon electrodes in electrochemical devices due to its large surface area and high electrical conductivity. It has been used in prototype supercapacitors[55] and Li-ion batteries[56,57] and many further applications are proposed. Single graphene layers are detectable using Raman scattering and the Raman spectroscopy of graphene has become a standard method for graphene characterization.[58] The primary features in the Raman spectrum of graphene are the G band at 1582 cm^{-1} and the G′ band at about 2700 cm^{-1} (also called the 2D peak). In a disordered sample the D-band can also appear at about 1350 cm^{-1}.[58] The details of the Raman spectrum of graphene have been extensively investigated.[59] The lineshape and position of the G′ band along with the ratio of the G and G′ band intensities can be used to determine the number of layers in a graphene sample. The detailed shapes and positions of the graphene Raman lines have been found to change with

applied gating voltages, charge doping and molecular intercalation.[60-62] These results led us to study the Raman spectrum of graphene in electrolytes with applied voltages to determine how the graphene Raman spectra may provide information about the charging and structure of the electric double layer.

Graphene Raman spectra are usually measured by transferring the graphene onto a silicon wafer with ~300 nm thick SiO_2 surface layer. This substrate selection makes it easier to optically identify regions of single layer graphene.[63] Raman spectra from our instrument of single layer graphene on these SiO_2 substrates are shown in Figure 11.

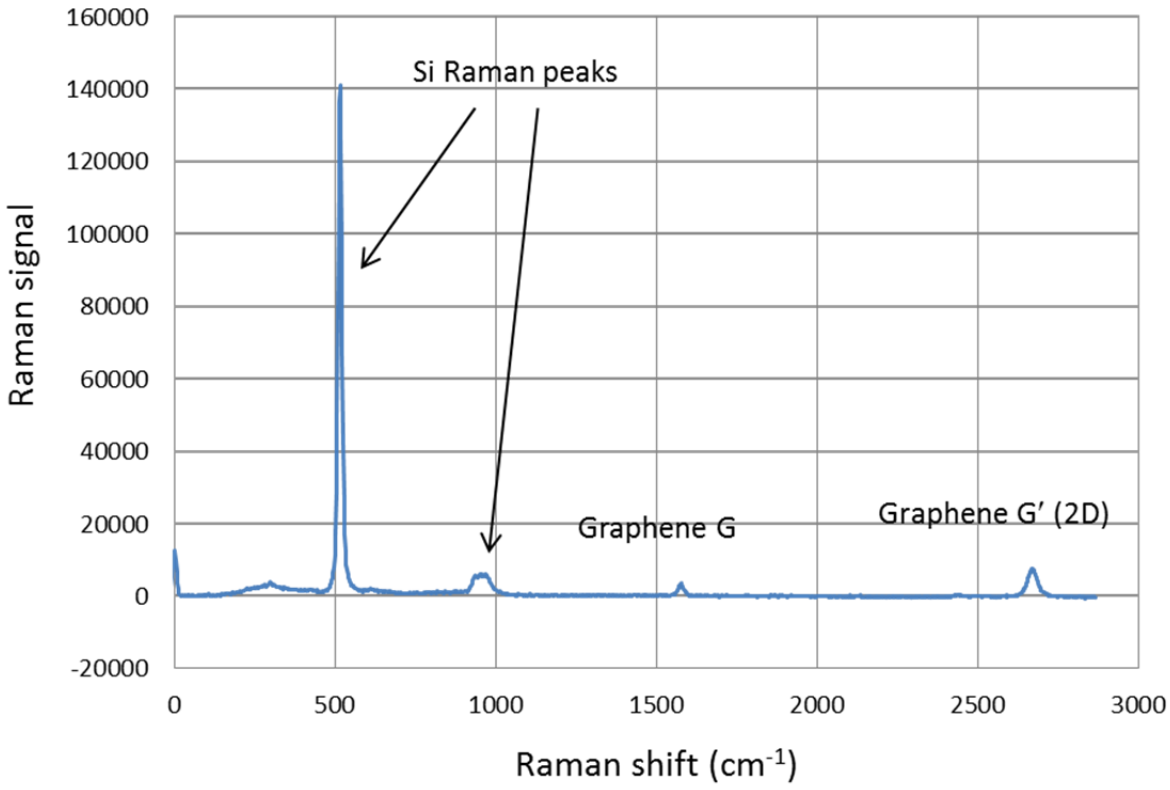

Figure 11. Raman spectrum of single layer graphene on SiO2/Si substrate.

To study graphene as an electrode material we need to measure Raman spectra of graphene as it is grown on metallic substrates. Graphene Raman spectra on metallic substrates have only very recently been studied. While the spectrum of graphene as commonly grown on copper is readily identifiable the measurements suffer from large backgrounds due to luminescence from the metal.[64] By experimenting with different Raman excitation wavelengths we were able to obtain low background spectra from commercial samples of CVD grown single layer graphene on

copper using 640 nm excitation. However the signal and background varies greatly from spot to spot on the samples. Raman spectra on commercial samples of graphene (Graphene Supermarket) grown on nickel substrates were also measured. These samples have ~1-7 layers of graphene with varying numbers of layers from spot to spot. However, they exhibit strong Raman spectra with little background using 532 nm excitation so they were used for initial studies with applied voltages in electrolyte solutions. Simple electrochemical cells were constructed with indium tin oxide coated coverslips serving as one electrode and as an optical window. The other electrodes were the commercial samples of graphene grown on nickel coated oxidized silicon wafers. The electrolyte was buffered aqueous $MgCl_2$. Raman spectra were measured through the indium tin oxide electrode and ~200μm of the electrolyte. The results are shown in Figure 12.

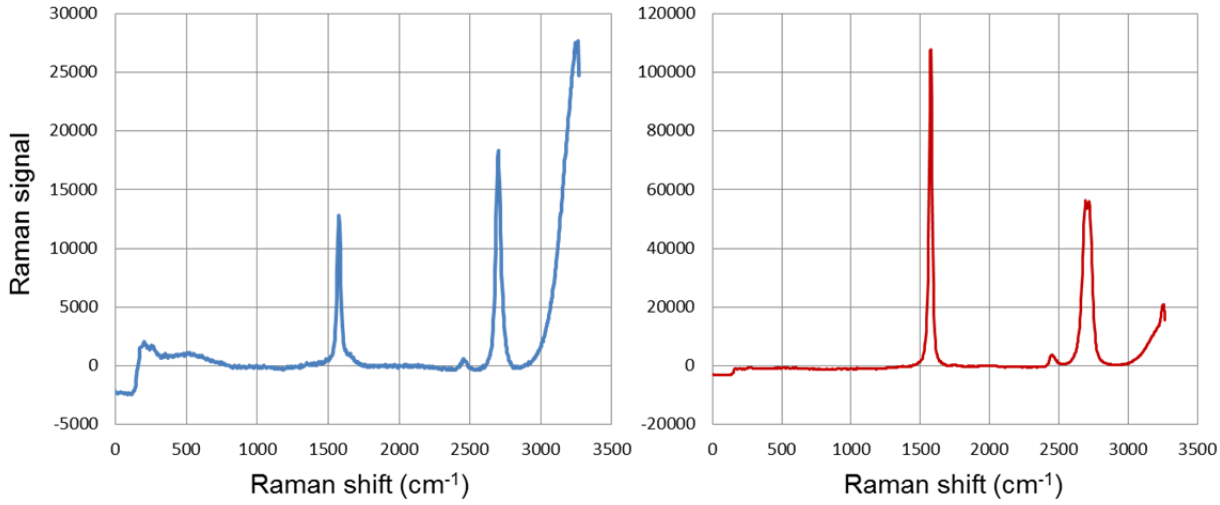

Figure 12. Raman spectra of graphene on Ni in MgCl2 electrolyte without and with applied voltage.
The graphene spectrum on the left is taken with no applied voltage. The spectrum on the right is taken several minutes after application of 1V with the graphene electrode negative. The rising signal on the right of each spectrum is water Raman signal.

The large change in the intensity and relative intensities of the graphene peaks upon applied voltage suggests that the electronic structure of the graphene changes leading to resonant enhancement of the Raman effect. Similar large changes in the intensities and relative intensities of the Raman peaks have been observed in investigations involving charge doping in experimental graphene field effect transistors.[60,62,65] In those experiments graphene charge doping is accomplished through polymer electrolytes either with directly applied gating voltages or with electrostatic backgating voltages applied through the silicon dioxide dielectric the

graphene rests on. Our experiments are among the first to use Raman spectroscopy to observe charging effects in liquid electrolytes as might be used in energy storage devices. The uncertainty in the height of graphene layer structures in our initial samples hampers detailed analysis, and the spectral effects of charging vary with position on the sample. Further study using graphene Raman spectra to observe electrochemical charging effects is very promising, but improved characterization and control of the graphene structure on metallic samples is needed.

8. FEMTOSECOND LASER SURFACE SECOND HARMONIC GENERATION ON ELECTROCHEMICAL INTERFACES

Surface second harmonic generation (SHG) measurements have been used for many years to investigate processes occurring during the charging and discharging of electrochemical interfaces.[66-73] Second harmonic generation in general requires a noncentosymmetric medium. An interface between two centosymmetric materials breaks this symmetry and thus SHG can occur at the interface. Since the symmetry breaking occurs within a few molecular layers at the interface, SHG is a highly specific probe of the interfacial region. The introduction of an electric field can enable SHG from an otherwise centrosymmetric medium through polarization of the material. This process is denoted electric field induced second harmonic (EFISH). If a strong electric field is present at an interface this can make an additional contribution to the interfacial SHG. The EFISH contribution to the overall nonlinear polarization at the second harmonic frequency can be written as:

$$\mathbf{P}_{EFISH}(2\omega) = \chi^{(3)} : \mathbf{E}_{DC} : \mathbf{E}(\omega) : \mathbf{E}(\omega)$$

where $\chi^{(3)}$ is the nonlinear susceptibility for three electric fields, in this case two at frequency ω and the DC field.[66] The contribution of this term to the SHG intensity is proportional to the square of the DC field. Thus if the DC electric field is the dominant source the SHG intensity should be quadratic in the DC electric field. In this case the SHG intensity can be used to monitor the surface charge density as a function of electric field.[67,68] For a number of interfacial systems the quadratic dependence of SHG intensity as a function of applied electric has been observed.[71] However, in many cases the voltage dependence of SHG is more complex, either because other sources of SHG are dominant or because other chemical processes occur.

Our new high-power, high-repetition-rate, femtosecond laser makes it possible to acquire very high signal-to-noise SHG data quickly. The high instantaneous intensity of the femtosecond pulse greatly enhances the efficiency of the nonlinear SHG signal production. This capability provides the opportunity to attempt the use of SHG to experimentally observe details of the layer by layer interfacial charging process predicted by our new molecular dynamics modeling results from this project. For this purpose we have assembled a SHG spectrometer using excitation by the amplified femtosecond laser pulses at 780 nm. The excitation pulse travels through a thin

electrochemical cell and is incident on the electrode surface of interest. The reflected beam from the surface is filtered to remove the fundamental wavelength and directed into a spectrometer with a linear CCD array detector. For experiments conducted so far the electrode of interest was gold deposited on a microscope slide. The opposite electrode is a transparent indium tin oxide coated cover slip. With a 1M NaCl electrolyte a strong SHG signal is detected. The SHG intensity has a substantial dependence on the applied voltage as shown in Figure 13.

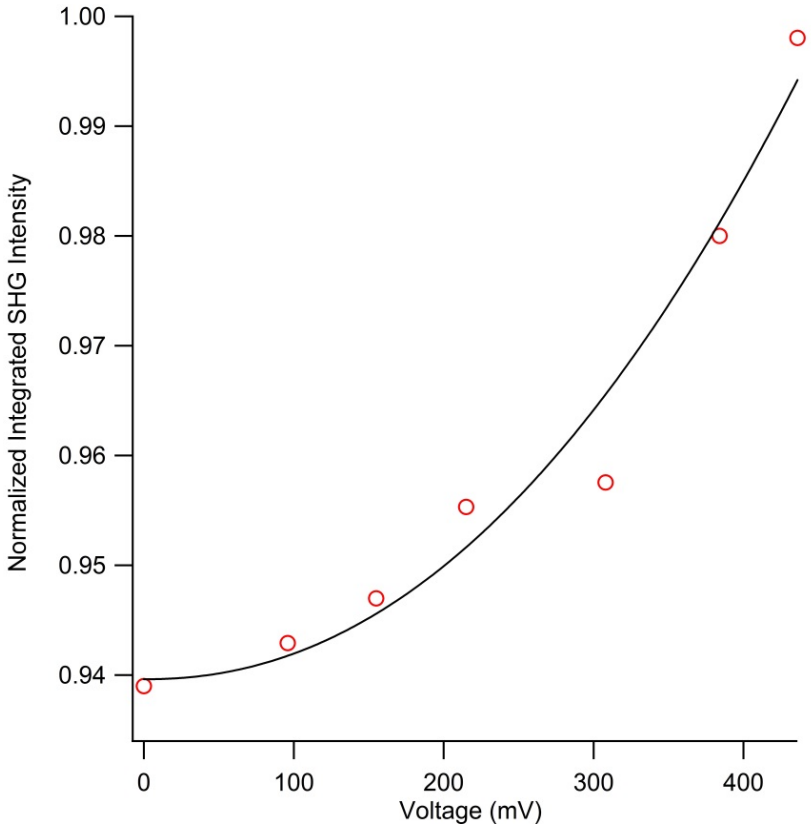

Figure 13. SHG signal intensity from a gold electrode in 1M NaCl as a function of applied voltage.

However, there is also a strong signal that does not appear to be voltage sensitive. In addition the spectrum of the second harmonic signal does not reflect the input spectrum, suggesting there is a resonant process contributing to the SHG. This resonance may possibly be due to adsorption of species to the gold surface. While detailed analysis of these results is incomplete they demonstrate that SHG signals are very readily obtained with our setup, and this is a promising route to directly observing details of the charging processes at electrochemical interfaces.

9. CONCLUSIONS

The theoretical component of this project has made important advancements in modeling electric double layer (EDL) structure. We developed a robust understanding of existing coarse-grained particle models in terms of packing structure and EDL capacitance, and demonstrated that these models over-predict EDL capacitance by a factor of 20 versus more realistic models. Going beyond existing simple models we have proven that molecular structure is important in the EDL to accurately predict capacitance based on the stability of intercalated molecules in condensed surface layers. In addition, we showed that the surface material can change EDL capacitance by over a factor of 2. To the best of our knowledge, we obtained the first direct characterization of the electrical medium near the electrode, which has a dielectric varying an order of magnitude from the bulk. Using this metric to separate diffuse and compact parts of the EDL greatly improves coarse-grained circuit models. Finally, we developed a simulation framework to rapidly build models supporting future prototyping based on molecular dynamics of different material systems. The experimental portion of this project has developed a sensitive confocal Raman microscope with a custom transmission grating spectrometer for surface vibrational spectroscopy. Results of an initial study of voltage dependent Raman spectra of graphene coated metallic electrodes in aqueous electrolytes suggest that charge doping of the graphene occurs in the field of the EDL. We have also implemented a polarization modulation reflection absorption infrared spectroscopy (PM-RAIRS) apparatus and used it to demonstrate vibrational spectroscopy of submonolayer components in model complex electrode surfaces. The PM-RAIRS apparatus provides the capability for species identification selective to interfaces. Finally, a new femtosecond laser enabled development of a surface-sensitive second harmonic generation spectrometer to study voltage dependent interfacial optical properties. Calculations of these optical properties are just becoming available from our theoretical modeling studies.

10. REFERENCES

1. Conway, B. E. *Electrochemical Supercapacitors*; Kulwer Academic: New York, **1999**.
2. Wang, H.; Laurent, P. *J. Phys. Chem. C* **2011**, *115*, 16711−16719.
3. Freund, J. B. *J. Chem. Phys.* **2002**, *116*, 2194−2200.
4. Qiao, R.; Aluru, N. R. *J. Chem. Phys.* **2003**, *118*, 4692−4701.
5. Thompson, A. P. *J. Chem. Phys.* **2003**, *119*, 7503−7511.
6. Qiao, R.; Aluru, N. R. *Phys. Rev. Lett.* **2004**, *92*, 198301.
7. Kim, D.; Darve, E. *Phys. Rev. E* **2006**, *73*, 051203.
8. Wu, P.; Qiao, R. *Phys. Fluids* **2011**, *23*, 072005.
9. Cui, S. T.; Cochran, H. D. *J. Chem. Phys.* **2002**, *117*, 5850−5854.
10. Feng, G.; Qiao, R.; Huang, J.; Sumpter, B. G.; Meunier, V. *ACS Nano* **2010**, *4*, 2382−2390.
11. Wander, M. C. F.; Shuford, K. L. *J. Phys. Chem. C* **2010**, *114*, 20539−20546.
12. Vanderlick, T. K.; Scriven, L. E.; Davis, H. T. *J. Chem. Phys*. **1989**, *90*, 2422−2436.
13. Tang, Z. X.; Mier-y-Teran, L.; Davis, H. T.; Scriven, L. E.; White, H. S. *Mol. Phys.* **1990**, *71*, 369−392.
14. Tang, Z.; Scriven, L. E.; Davis, H. T. *J. Chem. Phys*. **1992**, *97,* 494−503.
15. Gillespie, D.; Nonner, W.; Eisenberg, R. S. *Phys. Rev. E* **2003**, 68.
16. Wang, Z.; Liu, L.; Neretnieks, I. *J. Phys.: Condens. Matter* **2011**, 23.
17. Patra, C. N.; Ghosh, S. K. *J. Chem. Phys*. **2002**, *117*, 8938−8943.
18. Conway, B. *J. Electrochem. Soc.* **1991**, *138*, 1539−1548.
19. Harnett, C. K.; Templeton, J.; Dunphy-Guzman, K. A.; Senousy, Y. M.; Kanouff, M. P. *Lab Chip* **2008**, *8*, 565−572.
20. Srinivasan, S., *Bioelectrochemistry*; Springer: New York, **1985**; Vol. 10.
21. Sjöström, L.; Akesson, T.; Jönsson, B. *Ber. Bunsen-Ges. Phys. Chem*. **1996**, *100*, 889−893.
22. Hunter, R. J. *Foundations of Colloid Science, 2nd ed*.; Oxford University Press: Oxford, **2000**.
23. Nilson, R. H.; Griffiths, S. K. *J. Chem. Phys*. **2006**, *125* (16), 164510.
24. Lee, J. W.; Nilson, R. H.; Templeton, J. A.; Griffiths, S. K.; Kung, A.; Wong, B. M. *J. Chem. Theory Comput.* **2012**, *8*, 2012−2022.
25. Dani, J. *Biophys. J.* **1986**, *49*, 607−618.
26. Adcock, C.; Smith, G. R.; Sansom, M. S. P. *Biophys. J*. **1998**, *75*, 1211−1222.
27. Rostovtseva, T. K.; Aguilella, V. M.; Vodyanoy, I.; Bezrukov, S. M.; Parsegian, V. A. *Biophys. J.* **1998**, *75*, 1783−1792.
28. Stein, D.; Kruithof, M.; Dekker, C. *Phys. Rev. Lett*. **2004**, *93*, 035901.
29. Eigen, M.; Wicke, E. *J. Phys. Chem.* **1954**, *58*, 702−714.
30. Kralj-Iglic, V.; Iglic, A. J. *Phys. II France* **1996**, *6*, 477−491.
31. Lamperski, S.; Outhwaite, C. W.; Bhuiyan, L. B. *Mol. Phys.* **1996**, *87*, 1049−1061.
32. Borukhov, I.; Andelman, D.; Orland, H. *Phys. Rev. Lett.* **1997**, *79*, 435−438.
33. Fedorov, M. V.; Kornyshev, A. A. *Electrochim. Acta* **2008**, *53*, 6835−6840.
34. Wang, H.; Pilon, L. *J. Phys. Chem. C* **2011**, *115*, 16711−16719.
35. Henderson, D.; Jiang, D.; Jin, Z.; Wu, J. *J. Phys. Chem. B* **2012**, *116*, 11356−11361.
36. Plischke, M.; Henderson, D. J. *Chem. Phys*. **1988**, *90*, 5738−5741.
37. Spohr, E. *Electrochim. Acta* **1999**, *44*, 1697−1705.
38. Crozier, P. S.; Rowley, R. L.; Spohr, E.; Henderson, D. J. *Chem. Phys.* **2000**, *112*, 9253−9257.

39. Xu, D.; Li, D.; Leng, Y.; Chen, Y. *Mol. Sim*. **2007**, *33*, 959−963.
40. Willard, A. P.; Reed, S. K.; Madden, P. A.; Chandler, D. *Faraday Discuss*. **2009**, *141*, 423−441.
41. Blum, L.; Henderson, D. J. *Chem. Phys*. **1981**, *43*, 1901−1910.
42. MacDonald, J. R. *J. Electroanal. Chem.* **1987**, *223*, 1−23.
43. Bonthuis, D. J.; Gekle, S.; Netz, R. R. *Phys. Rev. Lett.* **2011**, *107*, 166102
44. Gouy, L. *J. Phys. Theor. Appl.* **1910**, *9*, 457.
45. Chapman, D.L., *Philosophical Magazine Series 6* **1913**, *25*, 475.
46. Stern, O., *Elektrochemistry* **1924**, *30*, 508.
47. Kilic, M. S.; Bazant, M. Z.; Ajdari, A. *Physical Review E* **2007**, *75*, 021502.
48. Dahanayaka, D. H; Wang, J. X.; Hossain, S.; Bumm, L.A. *J. Am. Chem. Soc*. **2006**, *128*, 6052-6053.
49. Chidsey, C. E. D.; Loiacono, D. N.; *Langmuir* **1990**, *6*, 682-691.
50. Finklea, H.O. in: Electrochemistry of Organized Monolayers of Thiols and Related Molecules on Electrodes, in: Bard, A.J.; Rubinste I. (Eds.), Electroanalytical Chemistry, vol. 19, Marcel Dekker, Inc., New York, 1996.
51. Krysiński, P.; Brzostowska-Smolska, M. *Bioelectrochem. Bioenerg*. **1998,** *44*, 163-168.
52. Niu, L.; Kvarnström, C.; Ivaska, A. *J. Electroanal. Chem*. **2007,** *600*, 95-102.
53. Oklejas, V.; Sjostrom, C.; Harris, J. M. *J. Phys. Chem. B* **2003,** *107,* 7788-7794.
54. Novoselov, K. S.; Geim, A. K.; Morozov, S. V.; Jiang, D.; Zhang, Y.; Dubonos, S. V.; Grigorieva, I. V.; Firsov, A. A. *Science*, **2004**, *306*, 666-669.
55. Lee, H.; Kang, J.; Cho, M. S.; Choi, J-B.; Lee, Y. *J. Mater. Chem.* **2011**, *21*, 18215.
56. Kim, H.; Kim, S. W.; Park, Y. U.; Gwon, H.; Seo, D. H.; Kim, Y.; Kang, K. *Nano Res.* **2010**, *3*, 813–821.
57. Lin, J.; Peng, Z.; Xiang, C.; Ruan, G.; Yan, Z.; Natelson, D.; Tour, J. M. *ACS Nano* **2013**, *7*, 6001-6006.
58. Malard, L. M.; Pimenta, M. A.; Dresselhaus, G.; Dresselhaus, M. S. *Physics Reports* **2009**, *473*, 51-87.
59. Ferrari, A. C.; Basko, D. M. *Nature Nanotechnology* **2013**, *8*, 235-246 and references therein.
60. Das, A.; Pisana, S.; Chakraborty, B.; Piscanec, S.; Saha, S. K.; Waghmare, U. V.; Novoselov, K. S.; Krishnamurthy, H. R.; Geim, A. K.; Ferrari, A. C.; Sood, A. K. *Nature Nanotechnology* **2008**, *3*, 210-215.
61. Basko, D. M,; Piscanec, S.; Ferrari, A. C. *Phys. Rev. B* **2009**, *80*, 165413.
62. Kalbac, M.; Reina-Cecco, A.; Farhat, H.; Kong, J.; Kavan, L.; Dresselhaus, M. S. *ACS Nano* **2010**, *4*, 6055-6063.
63. Yoon, D.; Moon, H.; Son, Y-W.; Choi, J. S.; Park, B. H.; Cha, Y. H.; Kim, Y. D.; Cheong, H. *Phys. Rev. B* **2009**, *80*, 125422.
64. Costa, S. D.; Righi, A.; Fantini, C.; Hao, Y.; Magnuson, C.; Colombo, L.; Ruoff, R. S.; Pimenta, M. A. *Solid State Commun*. **2012**, *152*, 1317-1320.
65. Das, A.; Chakraborty, B.; Piscanec, S.; Pisana, S.; Sood, A. K.; Ferrari, A. C. *Phys. Rev. B* **2009**, *79*, 155417.
66. Lee, C. H.; Chang, R. K.; Bloembergen, N. *Phys. Reu. Lett.* **1967,** *18*, 167.
67. Corn, R. M.; Romagnoli, M.; Levenson, M. D.; Philpott, M. R. *J. Chem. Phys.* **1984**, *81*, 4127.

68. Corn, R. M.; Romagnoli, M.; Levenson, M. D.; Philpott, M. R. *Chem. Phys. Lett*. **1984**, *106*, 30.
69. Rojhantalab, H. M.; Richmond, G. L. *J. Phys. Chem*. **1989**, *93*, 3269.
70. Robinson, J. M.; Richmond, G. L. *Electrochim. Acta*. **1989**, *34*, 1639.
71. Guyot-Sionnest, P.; Tadjeddine, A. *J. Chem. Phys*. **1990**, *92*, 734.
72. Tadjeddine, A,; Guyot-Sionnest, P. *J. Phys. Chem*. **1990**, *94*, 519.
73. Corn, R. M.; Higgins, D. A. *Chem. Rev.* **1994**, *94*, 107-125.

DISTRIBUTION

1	MS9055	Christopher J. Kliewer	8353
1	MS9055	Carl C. Hayden	8353
1	MS9055	Thomas B. Settersten	8353
1	MS9292	Darryl Y. Sasaki	8621
1	MS9403	Marie Kane	8223
1	MS9403	Karla R. Reyes	8223
1	MS9957	Reese E. Jones	8256
1	MS9957	Jeremy A. Templeton	8365
1	MS0899	Technical Library	9536 (electronic copy)
1	MS0359	D. Chavez, LDRD Office	1911


Sandia National Laboratories